SUPPLEMENTARY INFORMATION FOR

Tuning the Surface States of Fe_3O_4 Nanoparticles for Enhanced Magnetic Anisotropy and Induction Efficacy

Kyle A. Portwin[a,b] *, Pablo Galaviz[c], Xiaoning Li[a], Chongyan Hao[a], Lachlan A. Smillie[a], Mengyun You[a], Caleb Stamper[a], Richard A. Mole[c], Dehong Yu[c], Kirrily C. Rule[b,c], David L. Cortie[b,c] & Zhenxiang Cheng[a] *

[a] Institute for Superconducting and Electronic Materials, Faculty of Engineering and Information Science, University of Wollongong, Innovation Campus, Squires Way, North Wollongong, NSW 2500, Australia

[b] School of Physics, Faculty of Engineering and Information Science, University of Wollongong, Wollongong, NSW 2522, Australia

[c] Australian Centre for Neutron Scattering, Australian Nuclear Science and Technology Organization, Lucas Heights, NSW 2234, Australia

* Email: kyleportwin@gmail.com * Email: cheng@uow.edu.au

Synchrotron Rietveld Refinements

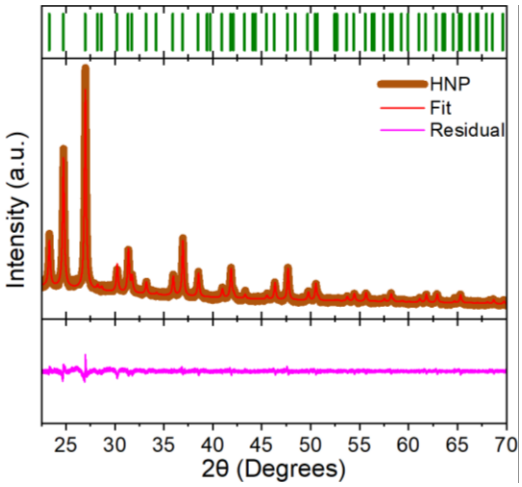

Figure S1. Rietveld refinement of HNP with planes of reflection above, and a residual of fit subtracted from experimental data below.

Fig S1. Presents the Rietveld refinement of HNP and table S1 shows the refinement parameters and weight factors. As mentioned in the main text, a reduction in lattice parameter is accompanied by an increase in microstrain after heat-treatment, indicating a greater volume of the maghemite (γ-Fe_2O_3).

Table S1. Rietveld refinement parameters and weight factors.

Parameter	UNP	HNP
GOF	1.87	1.42
R (%)	4.95	4.26
w_R (%)	6.63	5.37
χ^2	84909.8	49135.8
(a=b=c) (Å)	8.37218(6)	8.36017(7)
Particle size	16.4(1)	16.3(1)
Microstrain	-2796.3	-3466.9

To determine the thickness of the γ-Fe_2O_3 shell we must correspond the lattice parameter value to the volume of γ-Fe_2O_3 vs Fe_3O_4. This is done by A. Cervellino *et. al.* in Figure 2 of [1]. For a 16 nm particle, let the total radius = R = 8 nm and the core radius = r_c so that the total volume is $\mathbf{V_t} = \frac{4}{3}\boldsymbol{\pi}\mathbf{R^3}$ and the core volume is $\mathbf{V_c} = \frac{4}{3}\boldsymbol{\pi}\mathbf{r_c^3}$. The volume fraction of the

core is $\frac{V_c}{V_t} = \left(\frac{r_c}{R}\right)^3$. For our UNP lattice parameters, we can extrapolate from Figure 2 of [1] and find that $\frac{V_c}{V_t} = \mathbf{0.6}$. So, $\left(\frac{r_c}{R}\right)^3 = \mathbf{0.6}$. Solving for r_c: $\frac{r_c}{R} = (\mathbf{0.6})^{\frac{1}{3}} \approx \mathbf{0.843} \rightarrow \mathbf{r_c = 0.843 \times 8\ nm \approx 6.768\ nm}$.

The total thickness of the γ-Fe_2O_3 shell is $\mathbf{R - r_c = 8 - 6.768 = 1.232\ nm}$. One can also find that for HNP, with $\left(\frac{r_c}{R}\right)^3 = \mathbf{0.38}$, the γ-$Fe_2O_3$ shell thickness is 2.205 nm.

We show here that even though the sample may have a large contribution from γ-Fe_2O_3, physically this only corresponds to a very thin shell on the nanoparticles. The key is in the surface-volume ratio. After heat treatment we see the γ-Fe_2O_3 shell thickness increase by ~1 nm, which is a significant difference.

Neutron Inelastic Rietveld Refinements

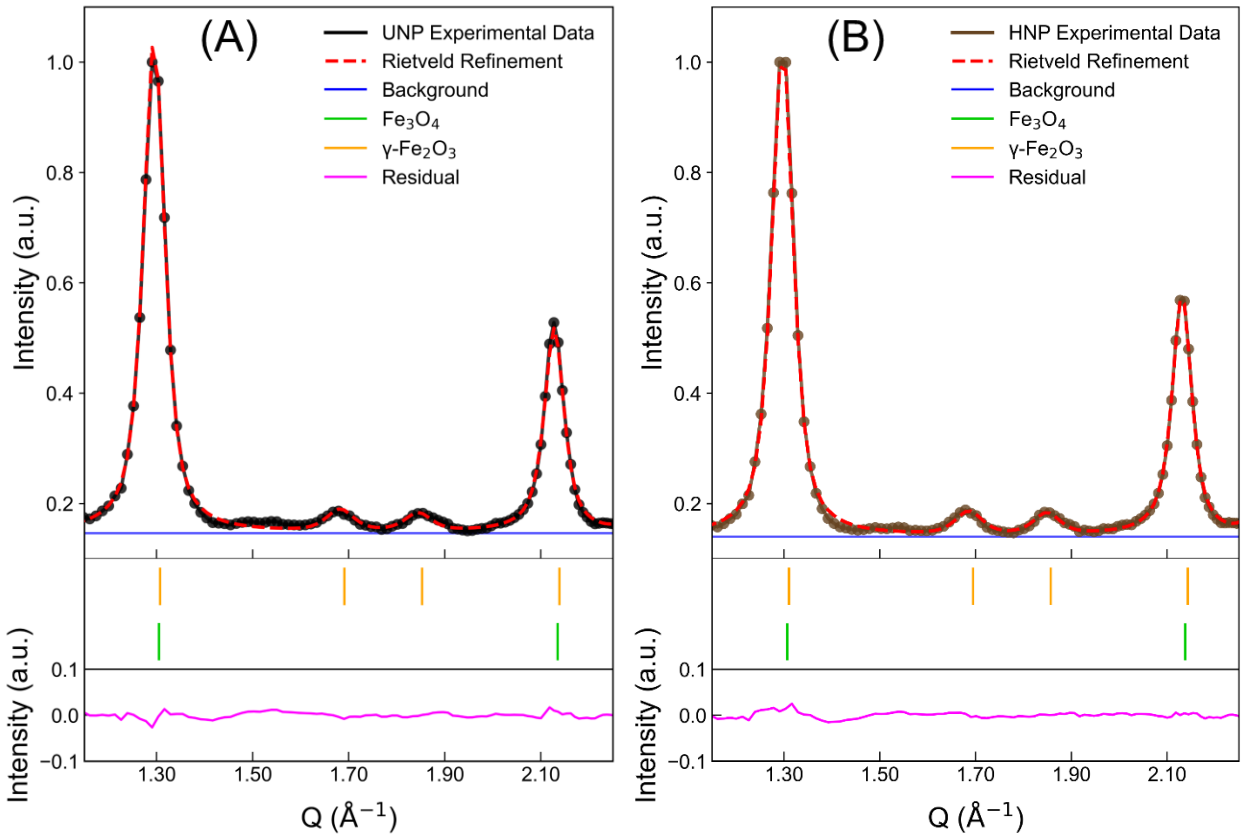

Figure S2. Inelastic neutron scattering with Rietveld refinements for (A) UNP and (B) HNP. Below the data and refinements are the tick marks for the Fe_3O_4,[2] and γ-Fe_2O_3,[3] phases, followed by the residual plot of refinements subtracted from the experimental data. Experimental data are normalized by the most intense reflection to 1.

Rietveld refinements of the elastic signal from time-of-flight inelastic neutron scattering, functionally equivalent to neutron powder diffraction, reveals clear structural differences between UNP and HNP. We perform refinements of UNP and HNP, Fig. S2(A) and 2(B), respectively, at 200 K to reduce the background signal from water. The refinements were conducted with key structural parameters constrained to isolate meaningful differences in phase composition and lattice parameters. For both refinements, the particle size was fixed at 16 nm and microstrain held constant at 1000, while instrumental and sample-dependent parameters were kept uniform to eliminate external sources of variability. The only free parameters in these fits were the phase fractions and the cubic lattice parameters of Fe_3O_4 and γ-Fe_3O_4. This refinement is challenging due to the substantial peak overlap between Fe_3O_4 and γ-Fe_2O_3, two Bragg reflections are shared by both phases, while only two reflections are unique to γ-Fe_2O_3. It is also not standard practice to refine the elastic signal from TOF-INS due to the large wavelength, lower resolution (compared to X-ray techniques) and difficult instrument parameters. The refinements here are therefore quite limited. Despite this, the refinements resolve the dominant phase as Fe_3O_4 in both samples, as evidenced by the high weight fractions of 87.6(4)% and 86.2(5)% for UNP and HNP, respectively, presented in Table S2. This majority Fe_3O_4 content is also reflected in the refined lattice parameters, which remain closer to the expected bulk value for Fe_3O_4 (8.396 Å) than for γ-Fe_2O_3 (8.33–8.35 Å). In the HNP sample, the increased γ-Fe_2O_3 content is indicated by both a higher weight fraction and a decrease in the refined lattice parameters, consistent with the incorporation of a greater proportion of the oxidized spinel phase. These results confirm that the nanoparticles a majority Fe_3O_4 core with γ-Fe_2O_3 shell, and heat-treatment induces and increase in γ-Fe_2O_3, leading to measurable shifts in both weight fractions and lattice parameters.

Table S2. Rietveld refinement parameters

	UNP	HNP
wR	2.54%	2.18%
R	2.04%	1.99%
Fe_3O_4 weight fraction	87.6(4)%	86.2(5)%
Fe_3O_4 lattice parameter (a = b = c)	8.3918(23) Å	8.3794(16) Å
γ-Fe_2O_3 weight fraction	12.4(4)%	13.8(5)%
γ-Fe_2O_3 lattice parameter (a = b = c)	8.375(14) Å	8.357(11) Å

S(Q,ω) Map. Fig. S3 presents the QENS signal for water at room temperature to compare with the QENS of the Fe_3O_4 nanoparticle samples. There is an absence of any Bragg peaks in the S(Q) plot, due to the liquid dynamics of the water. Notably, the QENS signal continues to grow as Q is increased, whereas in the nanoparticles, the QENS begins to flatten, suggesting there is some additional signal from other hydrogen and/or hydroxyl groups such as FeOOH.

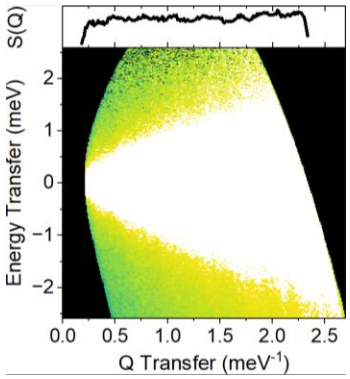

Figure S3. S(Q,ω) map for H_2O at room temperature.

QENS Analysis. It is standard in QENS analysis to plot the FWHM (meV) against Q^2 (Å^{-2}) and the Elastic Incoherent Structure Factor (EISF) (a.u.) against Q (Å^{-1}), Fig. S4A and S4B display this analysis, respectively. Firstly, it is important to note that there are false signals in the QENS where there are Bragg peaks and acoustic modes. In Fe_3O_4/γ-Fe_2O_3, Bragg peaks appear at 1.3 Å^{-1}, 1.7 Å^{-1}, 1.85 Å^{-1} and 2.1 Å^{-1}, which is why the corresponding results here don't follow the natural trend. Results are also skewed at low Q in the 200 K samples, including a peak at ~0.3 meV. This is a spurious feature from the cryofurnance on Pelican, so should be ignored.

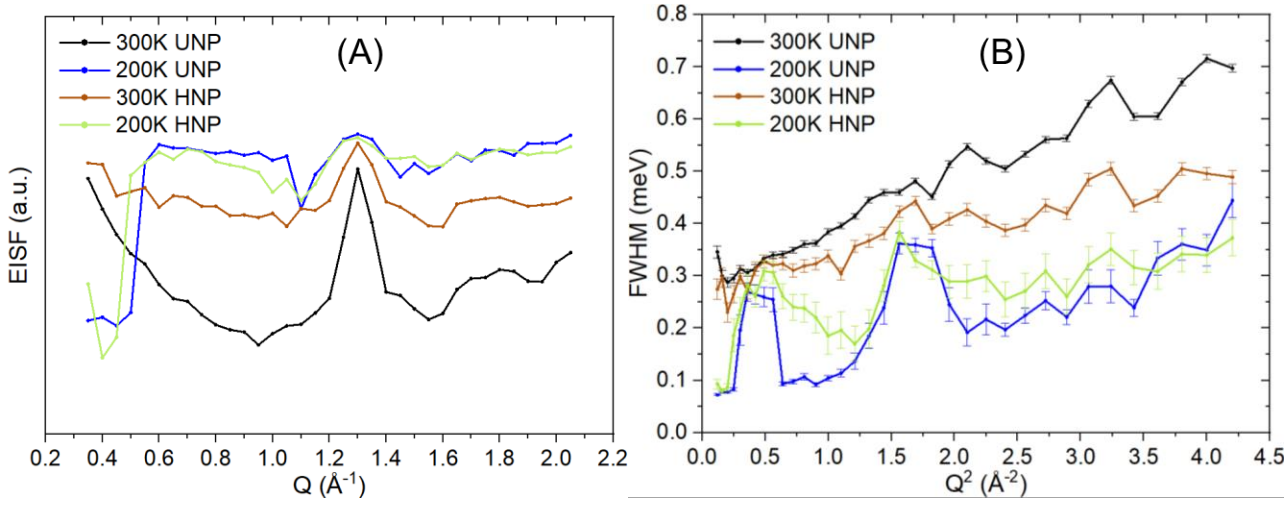

Figure S4. QENS analysis, (A) plots the FWHM against Q^2 and (B) shows the EISF against Q.

At 300 K, the FWHM appears to increase linearly with respect to Q^2 at low values. In UNP the FHWM continues to grow, whereas the HNP begins to flatten out. The linear increase is characteristic of liquid-like diffusion dynamics. When the FWHM

begins to flatten, this is a sign that there is rotational or confined diffusion, as opposed to long-range diffusion. At 200 K the signals from both samples are quite contaminated by the spurious feature and Bragg peaks, however it does appear flatter than the room temperature samples, which is expected.

The EISF data shows a much clearer picture than FWHM data. A flat EISF corresponds to localized motion or rotational diffusion, while an exponential decay indicates the presence of long-range translational diffusion. There is a clear difference here between the UNP at 300 K, which has an exponential decay, until reaching the Bragg peak at 1.3 $Å^{-1}$, and all other samples/temperatures which show a flat EISF. Interestingly, we can see that the exponential decay in UNP at 300 K does not continue after the Bragg peak, which tells us at short lengths, rotational or localized diffusion begins to dominate.

Imaginary AC susceptibility in an external DC field. Fig. S5 presents the temperature dependent χ'' of UNP and HNP at different frequencies and applied external DC fields. The low-temperature peak in UNP, which is evident across all frequencies, shifts slightly to lower temperatures when an external DC magnetic field is applied. This subtle shift suggests that the low-temperature peak corresponds to a clustered-spin-glass transition. Spin glasses are characterised by disordered and frustrated spin interactions, where clusters of spins freeze into a non-equilibrium state at low temperatures. When an external field is applied, the spins partially align with the field, reducing random spin fluctuations, so a lower temperature is required to freeze the spins into random orientations [4, 5]. In contrast, the high-temperature peak in χ'', associated with the superparamagnetic relaxation of nanoparticles, shows a dramatic shift to higher temperatures with increasing external field strength. The superparamagnetic phase is characterised by spontaneous spin-flipping events in the magnetic nanoparticles. When an external field is applied the spins align with the field, stabilising the energy barriers associated with magnetic anisotropy. This means a higher temperature is required to provide the spins enough thermal energy to overcome the increased anisotropy barriers. We can also clearly see here that the HNP have a higher magnetic anisotropy as they naturally have a higher blocking temperature [6,7]. Both the low-temperature spin glass and high-temperature superparamagnetic peaks exhibit these field-induced shifts across the frequency range studied.

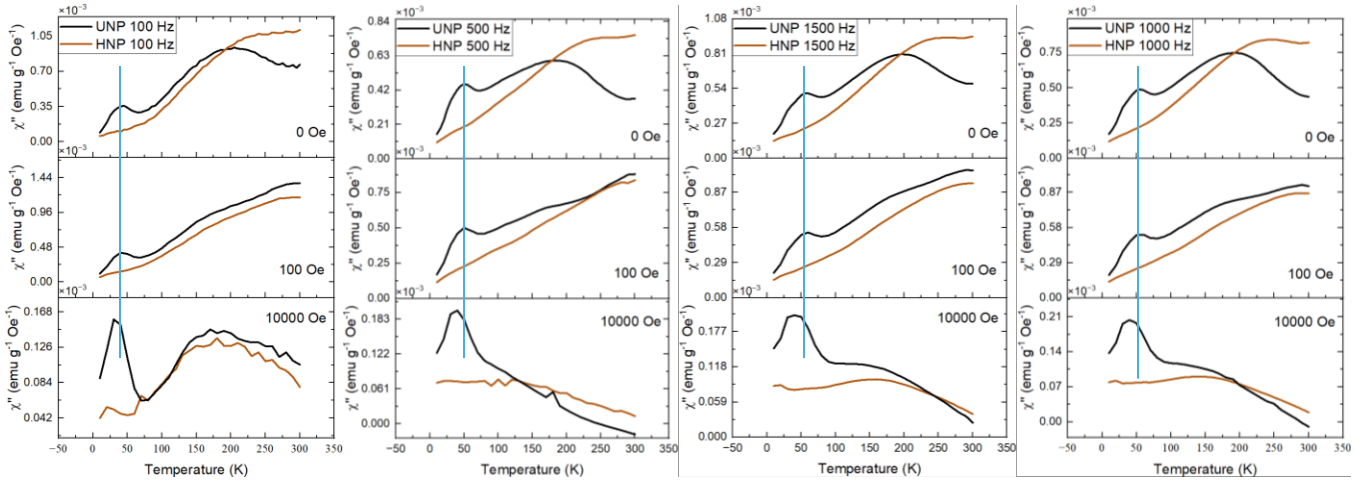

Figure S5. Imaginary susceptibility as a function of temperature at different frequencies and applied DC fields for UNP and HNP. The blue line highlights the shift in peak position with applied field.

REFERENCES

(1) Cervellino, A.; Frison, R.; Cernuto, G.; Guagliardi, A.; Masciocchi, N. Lattice parameters and site occupancy factors of magnetite–maghemite core–shell nanoparticles. A critical study. *Journal of Applied Crystallography* **2014**, *47* (5), 1755-1761. DOI: https://doi.org/10.1107/S1600576714019840.

(2) Haavik, C.; Stølen, S.; Fjellvåg, H.; Hanfland, M.; Häusermann, D. Equation of state of magnetite and its high-pressure modification: Thermodynamics of the Fe-O system at high pressure. *American Mineralogist* **2000**, *85* (3-4), 514-523. DOI: 10.2138/am-2000-0413 (acccessed 6/6/2025).

(3) Cvejic, Z.; Rakic, S.; Kremenovic, A.; Antic, B.; Jovalekic, C.; Colomban, P. Nanosize ferrites obtained by ball milling: Crystal structure, cation distribution, size-strain analysis and Raman investigations. *Solid State Sciences* **2006**, *8* (8), 908-915. DOI: https://doi.org/10.1016/j.solidstatesciences.2006.02.041.

(4) Binder, K.; Young, A. P. Spin glasses: Experimental facts, theoretical concepts, and open questions. *Reviews of Modern Physics* **1986**, *58* (4), 801-976. DOI: 10.1103/RevModPhys.58.801.

(5) Mydosh, J. A. *Spin glasses: an experimental introduction*; CRC Press, 1993.

(6) Dormann, J.-L.; Fiorani, D.; Tronc, E. Magnetic relaxation in fine-particle systems. *Advances in chemical physics* **1997**, *98*, 283-494.

(7) Goya, G. F.; Berquo, T.; Fonseca, F. C.; Morales, M. Static and dynamic magnetic properties of spherical magnetite nanoparticles. *Journal of applied physics* **2003**, *94* (5), 3520-3528.